The Astronomical Journal, 138:272–286, 2009 July doi:10.1088/0004-6256/138/1/272

RING EDGE WAVES AND THE MASSES OF NEARBY SATELLITES

John W. Weiss[1], Carolyn C. Porco[1], and Matthew S. Tiscareno[2]
[1] CICLOPS/Space Science Institute, Boulder, CO 80301, USA
[2] Cornell University, Ithaca, NY 14853, USA
Received 2008 September 29; accepted 2009 May 11; published 2009 June 11

ABSTRACT

Moons embedded in gaps within Saturn's main rings generate waves on the gap edges due to their gravitational disturbances. These edge waves can serve as diagnostics for the masses and, in some cases, orbital characteristics of the embedded moons. Although *N*-body simulations of the edges are far better in inferring masses from edge morphology, the long run-times of this technique often make it impractical. In this paper, we describe a faster approach to narrow the range of masses to explore with *N*-body simulations, to explore the multidimensional parameter space of edge/moon interactions, and to guide the planning of spacecraft observations. Using numerical, test-particle models and neglecting particle–particle interactions, we demonstrate that the simple analytic theory of the edge waves applies well to Pan in the Encke Gap but breaks down for smaller moons/gaps like Daphnis in the Keeler Gap. Fitting an analytic model to our simulation results allows us to suggest an improved relationship between moon-mass and edge wave amplitude. Numerical methods also grant freedom to explore a wider range of moon and ring orbits than the circular, coplanar case considered by analytic theory. We examine how pre-encounter inclinations and eccentricities affect the properties of the edge waves. In the case where the moon or ring-edge particle orbits initially have eccentric radial variations that are large compared to the gap width, there is considerable variation in edge wave amplitude depending on the orbital phase of the encounter. Inclined moons also affect the edge wave amplitude, potentially significantly, as well as generate vertical waves on the gap-edges. Recent Cassini images acquired as Saturn approaches equinox and the Sun's elevation on the ringplane is extremely low have revealed long shadows associated with the Keeler gap edge waves created by the embedded moon Daphnis. We interpret these as being cast by ∼1 km high vertical structure in the waves created by Daphnis' out-of-plane perturbations on the ring particles.

Key words: planets: rings

1. INTRODUCTION

To date, two moons have been discovered in gaps within Saturn's rings—Pan in the Encke Gap (Cuzzi & Scargle 1985; Showalter 1991) and Daphnis in the Keeler Gap (Porco & The Cassini Imaging Team 2005). However, there are many more gaps in the rings that are most easily explained by invoking as yet unseen moons inside them. One of the goals of the Cassini mission is to search for and determine the orbits of any such moons. Consequently, although they will be small, these moons can affect the dynamics of the rings, especially in angular momentum transport. Measurements of the masses of these moons are also helpful in unraveling their origins (Porco et al. 2007). In addition, gap–moons provide nearby dynamical analogs for planets in disks around other stars after the former have opened gaps.

Moons embedded inside rings cause radial variations on the edges of their gaps (Figure 1). In the simplest case, the moon and ring are coplanar and both have no orbital eccentricity pre-encounter.[3] In this case, the waves appear static in the moon's reference frame, although individual particles pass through the waves since their orbital frequency differs from that of the moon due to Kepler shear. Kepler shear also results in the waves having a 180° rotational symmetry—on the inner edge of the gap the waves lead the moon and on the outer they trail it, assuming that the ring characteristics (e.g., τ, ν, Σ) are similar on both edges and that the moon is centered in the gap.

The masses of many moons are best determined by their effects on other satellites or on rings since spacecraft flybys are often not feasible. Gap–moons (both those known and those inferred to exist) are generally too small to measurably perturb the other known moons or to affect distant parts of the rings,[4] but their effects on the gap-edges in their immediate areas can be significant and measurable. The usual method of determining mass of gap–moons begins with an analytic model for the ring edge's response to the perturbing moon. For a Keplerian disk, such as planetary rings, the amplitude of the edge waves is

$$ae = 2.24\mu \left(\frac{a}{\Delta a}\right)^2 a, \tag{1}$$

where a is the orbital semimajor axis of the moon, e is the induced orbital eccentricity so $(a \pm \Delta a)e \approx ae$ is the radial amplitude of the edge waves, μ is the ratio of the mass of the moon to the mass of the central planet, and Δa is the initial (upstream) absolute difference in moon and edge orbital semimajor axes, usually the same as the half-width of the gap since moons typically orbit in the center of their gaps. This expression was first derived by Julian & Toomre (1966) in the context of stars in a galactic disk. An alternate, shorter derivation can be found in Dermott (1984), although the latter gets a less accurate multiplicative constant, probably due to neglect of tangential forces on the ring particles. Both analyses assume that the ring particles approach the disturbing moon on initially

[3] For cases where the assumptions of coplanarity and circularity of the orbits break down, we shall see that the edge waves take on time-variable forms, although the basic description here roughly holds true.

[4] A notable exception is Pan, which raises numerous density waves in the rings (Porco et al. 2005; Tiscareno et al. 2007), but accurately inferring moon masses from density wave amplitudes remains problematic (Rosen et al. 1991; Jacobson & French 2004).

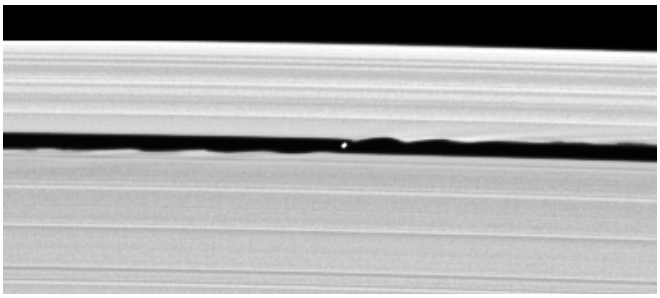

Figure 1. One of the discovery images of Saturn's ring–moon Daphnis in the Keeler Gap. The planet is roughly downward and the orbital direction is to the left in this orientation. (The figure has been reflected left-to-right to maintain this convention since this image was taken on the south side of the rings.) Daphnis is ~ 9 km (Porco et al. 2007) in diameter along its longest (radial) dimension and here the gap is 35 km wide (NASA/JPL/CICLOPS/SSI).

circular orbits and that the gap half-width is small compared to the orbital semimajor axis of the moon ($\Delta a/a \ll 1$) and that the change in the particle's semimajor axis, ΔX, is much smaller than Δa.

Goldreich & Tremaine (1982) also derive an expression ΔX. Recasting their expression in terms of variables used in this work,

$$\Delta X = \frac{2}{3}\frac{(ae)^2}{\Delta a}. \quad (2)$$

We can employ this to predict where the condition $\Delta X \ll \Delta a$ breaks down by taking the ratio of ΔX to Δa:

$$\frac{\Delta X}{\Delta a} = \frac{2}{3}\left(\frac{ae}{\Delta a}\right)^2. \quad (3)$$

Using Equation (1) and the definition of the Hill radius, $(\mu/3)^{1/3}a$, this becomes

$$\frac{\Delta X}{\Delta a} = 30.1\left(\frac{\Delta a}{R_H}\right)^{-6}. \quad (4)$$

Solving for Δa when $\Delta X/\Delta a \approx 0.01$, we get the critical $\Delta a \approx 3.8R_H$. As we will demonstrate, the Daphnis–Keeler system is near this cutoff, although $\Delta X/\Delta a$ falls off rapidly with Δa, making small changes significant.

Not only are potentially incorrect assumptions required to derive the analytic expressions above, they are restricted to the case where the orbits of the particle and moon are initially circular and coplanar. Ring–moons are now known to have nonzero eccentricities and inclinations (Spitale et al. 2006; Jacobson et al. 2008) and the Encke edge is known to display structure upstream of Pan (Porco et al. 2005; Tiscareno et al. 2005; Torrey et al. 2008), most likely due to the last encounter with the moon.

In this paper, we present a more accurate method to this problem: use of numerical integrations of particles passing the moon. Such integrations require fewer assumptions than the analytic model described above, improving the accuracy of the result. Additionally, the relaxed assumptions mean that we can treat cases where the particles and/or the moon have orbital eccentricities or inclinations before their encounter. This is a significant improvement since both Pan and Daphnis have nonzero eccentricities and Daphnis has a substantial inclination.

It should be emphasized that the numerical integrations presented here are not *N*-body simulations as they neglect particle–particle interactions (in particular, collisions and self-gravity). It is reasonable to ask, "what is the value of such simple computations in an era of *N*-body codes?" It is certainly true that for moons with large eccentric variations relative to their gap widths, the methods used in this work do not give sufficiently accurate models of the ring edges to determine the moon mass. As we will show, in situations with an eccentric moon (like Daphnis), collisions—often between particles with very different velocities—will become too common in the first wavelength of the edge waves to neglect such interactions. However, the approach we describe here is not without utility.

In cases where the moon and edges approach each other on low-eccentricity orbits (i.e., pre-encounter $ae \ll \Delta a$), we will show that our methods and our fit (Section 3.1) are quite adequate for determining the mass of the moon. *N*-body simulations require far more time and computation resources than our methods making them wasteful in cases where the simpler models should yield comparable results.

Building on the above point, *N*-body models require an estimate of the moon's mass as a starting point for the simulations. We will show that the analytical technique used in the past is sufficiently inaccurate—tens of percent—as to start the *N*-body models quite far from the actual mass. Rectifying this error takes time and computing power that we feel could be saved by using our improved semianalytic estimates.

Additionally, it is not certain that orbits will be determined for all gap–moons yet to be discovered. Very small moons in narrow gaps are difficult to image: such observations require high-latitude geometries (to avoid foreshortening the gap), low phases (to see the moon), and high resolution (to ensure that the gaps are at least tens of pixels across). Observing opportunities that meet all of these requirements are rare. There is no guarantee that current missions—Cassini, in particular—will ever be able to acquire enough observations to fit an eccentric and/or inclined orbit accurately. In fact, we may not even acquire many views of the edge waves themselves. In such cases, *N*-body simulations are likely unnecessary when a simple semianalytic model will give essentially the same accuracy within the observational limits.

2. METHODS

In order to better study the interaction between moon and gap-edge, we integrate the equations of motion for ring particles as they pass the perturbing moon for a variety of initial conditions. We begin our investigation with the classical case where the ring and moon orbits are coplanar and all bodies start out on circular orbits. This allows both a study of the accuracy of the analytic model (Equations (1) and (2)) and will give us improved mass estimates for Daphnis and Pan to use in subsequent stages. With the improved masses, we then address situations that the analytic model was unable to consider. In particular, we study cases where at least one body is inclined or eccentric prior to the encounter in order to better understand how these conditions might affect our mass estimates.

Our method is more precise than the approximations used by Showalter & Burns (1982). In that work, the authors demonstrated that, to a good approximation, any coplanar interaction between an eccentrically orbiting moon and an eccentrically orbiting particle can be reduced to an equivalent encounter where only the moon is eccentric. This greatly reduces the computational requirements needed to examine possible interactions since there are two fewer free parameters to consider. Showalter & Burns (1982) found that the errors

associated with their approximation were about 1% for their study of the F ring, although errors are likely to be larger for narrow gaps where ae is *not* many times smaller than Δa. Fortunately, computational power has increased enormously in the interim and running hundreds, or even thousands, of separate encounters is no longer prohibitive. Therefore, we avoid any errors that the Showalter and Burns approximation may introduce and do many more integrations instead.

2.1. Equations of Motion

It is standard procedure with problems involving low-eccentricity orbits to use a coordinate system which corotates about the central mass (in this case, Saturn) with the mean motion of the moon, n. In this frame, we define the origin to be at the mean location of the moon (the moon may have an eccentric orbit) and the x-axis to point radially away from the planet. The y-axis points in the direction of the particle's orbit, and the z-axis points normal to the orbital plane (in a suitably right-handed manner, naturally). Note that this frame is noninertial because it rotates with frequency n.

In this frame, the linearized equations of motion are (Hill 1878; Julian & Toomre 1966; Stewart 1991)

$$\ddot{x} = 3n^2x + 2n\dot{y} + F_x \tag{5}$$

$$\ddot{y} = -2n\dot{x} + F_y \tag{6}$$

$$\ddot{z} = -n^2z + F_z, \tag{7}$$

where $F_{x,y,z}$ are the accelerations on the ring particles due to the moon's perturbation. These equations are accurate to order e, the orbital eccentricity of the particle; since ring particles typically have eccentricities of the order of 10^{-5} or smaller, these equations are more than sufficiently accurate in this regime and are commonly used—in one form or another—in ring dynamics.

The acceleration due to the moon's influence is given by

$$\begin{aligned} F_{x_i} &= -\frac{\partial}{\partial x_i}\left(-\frac{\mathcal{G}m}{d}\right) \\ &= -\frac{\mathcal{G}m}{d^3}\Delta x_i, \end{aligned} \tag{8}$$

where x_i is x, y, or z; $\Delta x_i = x_{i,\mathrm{particle}} - x_{i,\mathrm{moon}}$ is the x, y, or z separation between moon and particle; $\mathcal{G}$ is Newton's Constant; m is the mass of the moon; and d is the total separation between the particle and the moon. Note that we will, in the general case, allow the moon to have a nonzero orbital eccentricity. In this case, the separations between particle and moon are inherently functions of time as well as position of the particle in our coordinate system.

A suitable rescaling can simplify these equations further. The usual method, which we will also adopt, is to use n for the timescale and the moon's Hill radius as the length scale. In this case, the equations become

$$\ddot{x} = 3x + 2\dot{y} - 3\frac{\Delta x}{d^3} \tag{9}$$

$$\ddot{y} = -2\dot{x} - 3\frac{\Delta y}{d^3} \tag{10}$$

$$\ddot{z} = -z - 3\frac{\Delta z}{d^3}. \tag{11}$$

Note that Equations (9)–(11) reduce to Hill's equations in the case where the moon's orbit is circular. However, as mentioned earlier, the moon will typically be on an eccentric orbit so that Hill's equations do not apply. When the particle is far from the moon and the force terms from the moon (i.e., the terms with d^{-3}) are small, we can solve the equations of motion to good accuracy:

$$x = X - e\cos(t + \psi) \tag{12}$$

$$y = Y + 2e\sin(t + \psi) \tag{13}$$

$$z = I\cos(t + \zeta), \tag{14}$$

where X is the difference between the moon and particle's semimajor axes (so that $\Delta a = |X(t = 0)|$), $Y = Y_0 - \frac{3}{2}Xt$ is the azimuthal offset between the moon's and particle's mean locations, ψ and ζ are phases at $t = 0$, and e and I are the orbital eccentricity and inclination, respectively. (The orbital eccentricity and inclination are scaled by $(\mu/3)^{1/3}$, the Hill radius over the orbital semimajor axis, to maintain the nondimensionality we have established.) These equations describe guiding center motion (in x and y) about a point which translates (in this reference frame) at a fixed rate of $3X/2$ due to Keplerian shear. The epicycle about the guiding center is a two-to-one ellipse (longer in the orbital direction). By convention, $\psi = 0^\circ$ is at periapse. The vertical motion is sinusoidal and decoupled from the in-plane motions, although without loss of generality, we will assume that the ring particles' (pre-encounter) plane defines the reference plane so that $I_p = 0^\circ$.

Since the ring–moons, like the ring particles, have orbital eccentricities that are much less than unity, Equations (9)–(11) without the force terms apply to the moon, so Equations (12)–(14) describe the moon's trajectory to good accuracy. Since we assume that the moon's guiding center is the origin of our coordinate system, in this specific case X and Y are zero and the moon does not experience shear. We will use these equations to track the location of the moon rather than integrate it directly since the effects of the individual ring particles on the moon are negligible.

2.2. Numerical Methods

To study the effects of the passage of particles by a nearby moon, we integrate the above equations using a fourth-order Runge–Kutta scheme (Press et al. 2002), chosen for its robustness and the ready availability of a well tested code. In this work, we only study the case of a ring edge interior to the moon's orbit, recognizing that the equations of motion are symmetric under the 180° rotation that would correspond to the outer gap edge. For the inner edge case, we start the moon 250 Hill radii upstream from the particle, more than enough to ensure that the particle is initially unaffected by the moon and therefore only gradually begins to sense the moon's gravity.

It should be made clear that these integrations are for test-particle dynamics: the moon's orbit is not altered by passing particles. This is a reasonable approximation since individual particles are much too small to cause noticeable effects on the moon. Additionally, these are not N-body simulations in

the sense that particles do not interact with each other. For cases where both the moon's and particle's pre-encounter eccentricities are small, collisions are unlikely to play an important role for the first several orbits. In this time interval, particle streamlines do not cross, leading to grazing collisions that do little to alter the motions of the particles. However, after the first few orbits, the particles collide more violently so that the collisions will have significant effects on the particles' motions. For our purposes here—determining the masses of the moons from the edge waves—it is sufficient to examine only the first few waves. So this analysis can ignore such effects.

Each possible run contains up to seven parameters: Δa, e_p, ψ_p, I_m, ζ_m, e_m, and ψ_m, where the subscripts p refers to the particle and m to the moon. (Of course, a given ψ or ζ parameter becomes irrelevant if the corresponding e or I is zero. In our simulations, this will often be the case for one or more parameters.) Since Δa is measured in Hill radii, it folds in both the actual measured separation between the initial orbital semimajor axes and the moon's mass. A typical run involves stepping through values of Δa over a reasonable range, from 2.5 Hill radii to 20 Hill radii. For $\Delta a \lesssim 2.5 R_H$, the particles "horseshoe" (Dermott & Murray 1981) rather than get past the moon and therefore are not part of the gap edges, while for $\Delta a \gtrsim 20 R_H$ the effects of the moon become too small to be of interest. So, for example, a run with an eccentric moon would require stepping through the range of encounter phases (that is, the phase when the mean longitudes are equal), doing a full sweep of Δa from 2.5 R_H to 20 R_H at each phase.

2.3. Analysis of Simulations

To determine the postencounter ae and Δa, we solve Equations (12)–(14) for the guiding-center variables in terms of the Cartesian coordinates. For example, the radial location of the guiding center and the orbital eccentricity are given by

$$X = 2(2x + \dot{y}) \tag{15}$$

$$e = \sqrt{(2\dot{y} + 3x)^2 + \dot{x}^2}. \tag{16}$$

Because the particles will be essentially unaffected by the moon at large downstream distances, we use these inversions to determine the location of the edge and the edge wave amplitude. Although it is probably unnecessary, because it is computationally fast and simple, we also average the particles' e and ΔX over several orbits far downstream of the moon to determine the postencounter quantities.

In order to derive accurate masses of the moons, we must determine from the simulations the values of ae and ΔX well after the encounter. How far downstream of the encounter should we go before we measure these quantities in the simulation? Particles need to be far enough from the moon that the moon's forces are negligible. Let us temporarily assume that ΔX is small so that the particle's orbit does not move significantly relative to the moon's. (In reality, particles always shift away from the moon in the circular–circular cases—as can be shown via the Tisserand relation—so that the following analysis provides an upper bound on the magnitude of the postencounter forces.) Since the Kepler shear is $3n/2$ and a complete orbit is $2\pi/n$, the particles on the edge move $3\pi\Delta a$ downstream every orbit (Showalter & Burns 1982). Thus, we can look at the ratios of the force components to the peak values as a function of distance downstream (in orbits) and Δa will cancel out completely, making our results generalizable to all Δa.

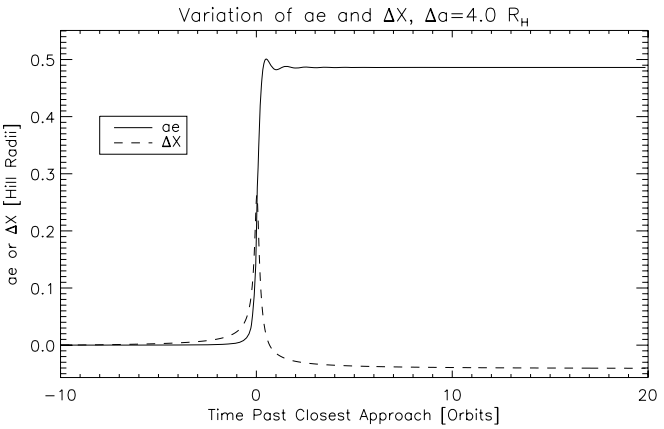

Figure 2. Variations of ae (solid line) and ΔX (dashed line) in Hill radii for a particle passing the moon at $\Delta a = 4 R_H$. Time zero is selected to be time of closest approach to the moon.

The magnitude of the force from the moon naturally peaks at closest approach and falls off rapidly with time in either direction. After one orbit, the force is down to just 1% of its peak value. The radial component of the force falls off even faster, dropping to 0.1% after a single orbit. The only component that does not fall off this rapidly is the tangential component of the force. This component is of great interest because it sets the torques and therefore (in this small-eccentricity limit) ΔX. Furthermore, this component does not peak at closest approach—where it is necessarily zero—but rather at $\pm 1/\sqrt{2}$ orbits from closest approach. One orbit downstream the tangential component of the force is only down to 3% of its peak value, still a potential concern if integrated over long times. Our approach, therefore, is to wait 10 orbits after the encounter to measure e and ΔX. At this point, the force components are down to 0.003% of their peak values or less.

Figure 2 shows a typical case of the time variations of ae and ΔX (both in Hill radii). Time 0 is at closest approach, so the time axis can be read as "orbits after closest approach." The figure shows that while there are noticeable transient behaviors immediately after passage, these die out after about five orbits. By 10 orbits after closest approach, both curves appear to have nearly reached their limiting values, so measuring ae and Δa at this time yields good results.

As for measuring actual edge waves from images, Figure 2 shows that while ae and ΔX are still evolving somewhat in the first few orbits, ae has already approached its final limiting value reasonably closely after one orbit. Since the change in ΔX after this time is small compared to the final value of ae, this means that measuring the edge wave amplitude in the first few waves (before collisions damp them out in real ring edges) is, in fact, sufficiently accurate to get good results.

Unfortunately, it is not always possible to measure the amplitudes of the edge waves seen in images as far downstream as we would like because collisions begin to destroy the simple edge wave behavior before this time. Dermott (1984) gives an estimate for the distance downstream when neighboring streamlines begin to cross and collisions begin to occur: $3(\Delta a)^2/(2(ae))$. However, this assumes that the neighboring streamlines have the same postencounter ae and that the first collisions occur many ($\gg 1$) orbits downstream. The expression can be expressed in terms of orbits downstream by dividing by the wavelength for

Figure 3. Figure 1 reprojected as if the observer were 90° above the ring plane. The image has also been remapped so that features at a constant ring radius are on a horizontal line and features on the same longitude are on a vertical line everywhere in the image. This facilitates measuring ring features. The image has been cropped and enlarged around Daphnis and stretched in the radial direction to enhance the visibility of the edge waves.

the edge waves: $3\pi\Delta a$, yielding streamline-crossings when

$$\text{Number of Orbits} = \frac{\Delta a}{2\pi(ae)}. \tag{17}$$

This result is identical to Equation (2.1.9) in Showalter et al. (1986), except that they yield longitude downstream rather than number of orbits. For the Pan–Encke system, the gradient in induced ae on the edge is small so that the above assumption is reasonable. In this case, Equation (17) says that collisions begin to really matter about 16 orbits after the encounter with Pan. Plotting separation between streamlines—allowing for the analytically predicted (Equation (1)) change in ae with Δa—and locating intersections by inspection shows this to be a good estimate. In the Daphnis–Keeler system, however, Δa is much smaller and ae varies more rapidly with increasing separation at the gap-edge. Equation (17) suggests that collisions should occur less than a full orbit after the encounter with Daphnis. A more accurate approach to finding the first streamline crossings in this situation is to plot the separations between streamlines—allowing for variations in ae—and locating intersections by inspection or numerical solution. Using Equation (1) to find the gradient in ae, this technique shows that streamlines go well over an orbit after encountering Daphnis before their first intersection. It is therefore reasonable to use the first few edge waves on the Keeler Gap in order to infer Daphnis' mass.

2.4. Data Analysis

To more precisely measure the edge wave amplitudes and gap half-widths, we require scans of the edges of the gaps. So, after reducing the Cassini images with the standard Cassini Imaging Science Subsystem Calibration software (Porco et al. 2004), we navigate the images to adjust the pointing and then reproject the images to remove the effects of observer elevation above the ring plane and to eliminate the effects of ring curvature. (Thus, a circular ring becomes a straight line in the reprojected image.) Figure 3 shows an example of a reprojected image.

From the reprojected image, radial scans are used to numerically locate the edges of the gaps at each longitude, building up a scan of the edge as a function of longitude. From these scans, it is relatively simple to measure the edge wave amplitudes and upstream gap-width. As indicated above, the measurements are done in the first few wavelengths after the satellite encounter, although the first peak is never used as it generally appears to be larger in amplitude than subsequent peaks in both data and in the numerical models, suggesting that this peak is still too close to the moon and particles are still experiencing significant accelerations from the moon. Measurements are not done further downstream because waves on the Keeler Gap show clear signs of dissipation due to particle collisions after this point.

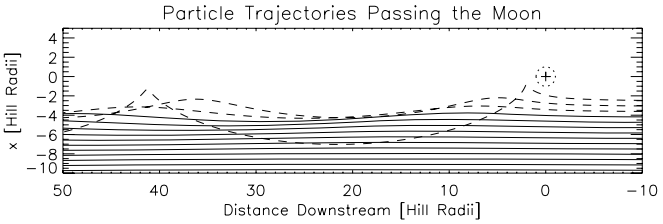

Figure 4. Trajectories for selected particles passing the moon. The dashed trajectories have $\Delta a < 4\ R_H$ while the solid trajectories have $\Delta a > 4\ R_H$. Units on both axes are Hill radii, the cross shows the location of the moon, and the circle delimits a one-Hill-radius zone around the moon. The planet is down in this view and the orbital direction is to the left.

Values of Δa and ae are reported in Table 1. For the Pan–Encke system, the measurements of Δa and ae appear to be consistent with time. The Daphnis–Keeler system is not so simple, however. The inner edge of the Keeler Gap is in a 32:31 inner Lindblad resonance with Prometheus, causing the edge's radial location to vary over a 15 km range (although the limited number of images analyzed here for the edge waves only see 7 km of variation). The outer edge, on the other hand, shows a much more consistent Δa range between 14 and 17 km. A further concern is that Daphnis's relatively large orbital eccentricity complicates measuring Δa. We use measurements of the edge separation to the location of Daphnis' semimajor axis, although for the circular–circular approximation this is not obviously the best method. In order to test this approach, we have examined the effect of using values of Δa found by measuring from the moon's instantaneous location to the edge and found that the reported range of masses inferred from the circular–circular approximation does not significantly change in this case. The values of ae also vary more on the inner edge than the outer edge, which is expected. Considering the differences in the edges, we have reported the Δa and ae values for the two edges separately in Table 1.

3. INITIALLY CIRCULAR ORBITS

Eccentricities of ring particles and ring–moons are small and all bodies have small orbital inclinations. Given this, it is sensible to begin our investigations with the case where $e_m(t = 0) = e_p(t = 0) = i_m(t = 0) = 0$. In this case, the only free parameter left to examine is Δa. Since this parameter is scaled by the Hill radius of the moon, varying it can be equivalent to varying either the difference in orbital semimajor axes of moon and particle or the mass of the moon. If we know the distance between the moon and the gap-edge reasonably well—which we typically do—a suite of runs with varying values of Δa can therefore be used to infer the mass of the central moon.

Figure 4 shows a selection of trajectories of particles as they pass the moon, scaled to Hill radii. As expected, the trajectories with larger values of Δa have smaller postencounter ae. For $\Delta a \gtrsim 4\ R_H$, the streamlines of the particles appear smooth and do not intersect. As Δa shrinks, however, the particles' ae after encounter grows larger and eventually the streamlines cut through each other at considerable angles. This implies relatively violent collisions between particles with large relative

Table 1
Useful Values for the Two Already Known Gap–Moons

Gap	Moon	a_{moon}(km)	Δa (km)	Wave Amp. (km)	Moon e	Moon I	$T_{synodic}$
Encke	Pan	133,584	161	1.6	1.44×10^{-5}	0.0001	319 days
					$\pm 0.54 \times 10^{-5}$	± 0.0004	(554 orbits)
Keeler	Daphnis	136,506	13–20 (inner)	1.8–5.4 (inner)	3.31×10^{-5}	0.0036	8.5 years
			14–16 (outer)	4.0–5.6 (outer)	$\pm 0.62 \times 10^{-5}$	± 0.0013	(5210 orbits)

Notes. Orbital data are taken from Jacobson et al. (2008), except the gap widths and edge wave amplitude of Pan (Porco et al. 2005) and the gap-width and edge wave amplitude of Daphnis (measured for this work). Measurements of the Keeler Gap show significant temporal variations, so we have quoted a range for the Δa (the absolute difference in moon and edge orbital semimajor axes) and ae. There is also a notable dynamical difference in the inner and outer edges of the Keeler Gap, so we have reported the ranges of Δa and ae separately here. Note that the smaller Δa corresponds to the larger ae and vice versa. Further measurements of the Keeler Gap's edge will be reported in a future paper by Tiscareno et al.

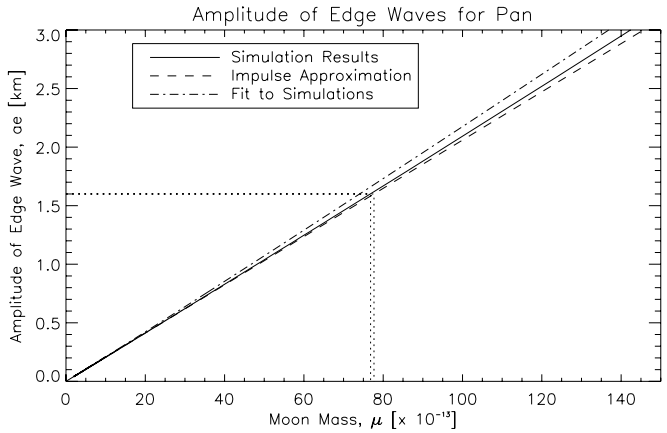

Figure 5. Amplitude of edge waves generated by Pan in the Encke Gap vs. the mass of that moon. Mass is given as a ratio of the mass of the moon to the mass of Saturn. The solid line shows the results of integrating the orbits of 5000 test particles while the dashed line shows the analytical predictions (Equation (1)). The dotted lines are used to show the interpolation from the observed amplitude of the edge waves on the Encke Gap (1.6 km) and the inferred moon masses for the two methods. The dot–dash line shows our fit to the numerical models (Section 3.1).

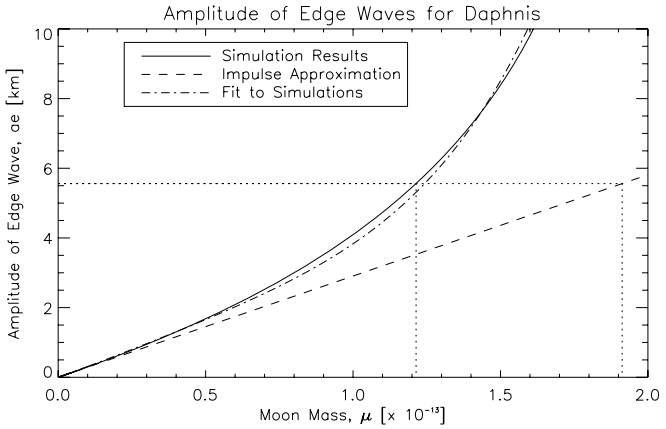

Figure 6. Amplitude of edge waves generated by Daphnis in the Keeler Gap vs. the mass of that moon. Curves are for $\Delta a = 14$ km, as measured to the outer edge of the Keeler Gap in images taken on 2007 April 25. As in Figure 5, mass is given as a ratio of the mass of the moon to the mass of Saturn. The solid line shows the results of our numerical simulations while the dashed line shows the analytical predictions (Equation (1)). The dotted lines are used to show the interpolation from the observed amplitude of the waves on the outer edge of the Keeler Gap (5.56 km) and the inferred moon masses for the two methods. The dot–dash line shows our fit to the numerical models (Section 3.1).

velocities (compared to the typical collision speeds in the rings), an effect we do not model and which we expect will change the morphology of the edges from what our models predict.

For example, the Encke Gap is separated from Pan by about 161 km, taking the average of the inner and outer edge separations from Porco et al. (2005). With this parameter fixed, we can create a relationship between simulated edge wave amplitude and mass of the moon. Figure 5 shows that the numerical results (solid line) agree with the analytical predictions (impulse approximation) fairly closely. The mass of Pan derived from Equation (1), using a wave amplitude (ae) of 1.6 km (Porco et al. 2005), is $\mu = 7.5 \times 10^{-12}$ (4.3×10^{18} g). This is in good agreement with the results of our numerical models, 7.8×10^{-12} (implying a Hill radius of 18.1 km); the two differ by 3%, which is smaller than the uncertainty caused by measurement errors. (Resolution in images used was slightly better than 1 km pixel^{-1} and the edge detection algorithm can locate an edge to within about 0.1 pixels. If the amplitude of the waves is 0.1 km larger or smaller than reported, the mass inferred would change by about 5%.) With the mass determined, we can also use the numerical results to measure how much the semimajor axis of the edge should change after the encounter: 0.14 km. This value is too small to observe with the current images. It is possible that with future data taken by Cassini or with a more careful analysis of the Encke Gap edge this prediction may be testable.

Although the Pan–Encke system showed little difference between the analytic theory and our numerical models, we might not expect the same from Daphnis–Keeler. Daphnis is much smaller than Pan (Porco et al. 2007) and much closer to the edge of the Keeler Gap (Porco et al. 2005). These two effects act against each other, the former tending to reduce the amplitudes of the edge waves, the latter tending to increase them. It is difficult to predict which of these effects will dominate, but observations show that distance wins: the amplitude of the edge waves varies from 1.8 to 5.6 km, generally much larger than seen on the edge of the Encke Gap.

The same suite of integrations used above can be applied to Daphnis by merely changing the moon-edge separation, although the circular–circular approximation is not likely to be nearly as robust here as it was in the Pan–Encke case. Using six pairs of Δa and ae (one each from the inner and outer edges taken from three imaging sequences, each sequence 8–16 months apart) to determine masses, we find a range in μ from 1.0×10^{-13} to 1.6×10^{-13} with a mean value of the six measurements of 1.2×10^{-13}, giving Daphnis a mass of 6.8×10^{16} g. Figure 6 shows the case of $\Delta a = 14$ km and $ae = 5.56$ km, a representative example. By comparison, the analytic models for these same measurements suggest a range of masses from $\mu = 1.3 \times 10^{-13}$ to $\mu = 2.4 \times 10^{-13}$, an average difference from our models of 35%.

The mean value of the mass we have found is surprisingly low when we consider that this implies a density of 0.28 g cm^{-3} while the analytically derived mass yields a density of 0.42 g cm^{-3} (Porco et al. 2007). Given that this density is well below what we would expect even for a porous, accreted moon, we believe that it is probable that there is nontrivial collisional damping of the edge waves even in the first few wavelengths. In the later sections of this paper where we investigate the effects of eccentricities and inclinations, we will therefore assume that Daphnis' mass is at the upper end of the range suggested, $\mu = 1.6 \times 10^{-13}$. This mass implies that Daphnis' Hill radius is 5.1 km, slightly larger than the moon's largest radius of 4.5 km (Porco et al. 2007).

Why do the analytic and numeric masses agree well for Pan, but not for Daphnis? Succinctly, the Keeler edge is much closer to Daphnis than the Encke edge is to Pan when measured in Hill radii, the most useful unit for this problem. Based on our numerical results, Δa in the Encke Gap is 8.8 Pan-Hill Radii while Δa in the Keeler Gap ranges from 3.0 to 4.3 Daphnis-Hill radii. Returning to Figure 4, trajectories with $\Delta a \gtrsim 4\ R_H$ (solid curves in figure) are weakly perturbed. In this region, the induced eccentricity in the particles' orbits is small compared to their separations from the moon so that the analytic model works well. However, in the "strongly disturbed" region, $\Delta a \lesssim 4\ R_H$ (dashed curves in figure), the eccentricity induced by the moon is enough to bring the particles significantly closer to the moon. This leads to larger accelerations on the particle than would occur otherwise and therefore further increases the induced eccentricities. This nonlinear feedback causes the deviation from the analytical prediction.

The significance of the deviations from the analytic theory goes beyond Daphnis and Pan. There are many gaps and edges in Saturn's rings which are considered good targets for moon searches and searches are indeed being carried out by Cassini's Imaging Science Subsystem (Porco et al. 2004). These gaps are often small, so that we may reasonably assume that the moons in them are only a few Hill radii away from the edges, more akin to Daphnis than to Pan. In this case, the actual masses of the moons are likely to be smaller than the prediction by 35% or more and the radii should be smaller by at least 15%.

3.1. Generalized Approximation to the Numerical Models

Since the linear analytic approximation for edge wave amplitudes fails to predict the edge wave amplitudes accurately, we should replace it with a (relatively) simple fit to the numerical models. Such a fit, although not derived from physical arguments, will be useful for determining moon masses from observations.

In Figure 7(a), we show the numerical models' relationship between the amplitude of the edge waves and Δa (in Hill radii) as a solid line. For much of the domain shown, the relationship is nearly linear in log–log space, indicating a reasonably good fit from a simple power law. However, for small Δa ($\lesssim 3\ R_H$) the slope is clearly much larger, necessitating a second component to our fit. Our first round of fitting used two power-law components. Exponents were determined by measuring the slopes in log–log space and coefficients were adjusted to fit the numerical simulations. It quickly became apparent that a third component was required for the intermediate Δa range, around 4 R_H. Thus, a third component was added. The resulting fit is shown in Figure 7(a) as a dashed line.

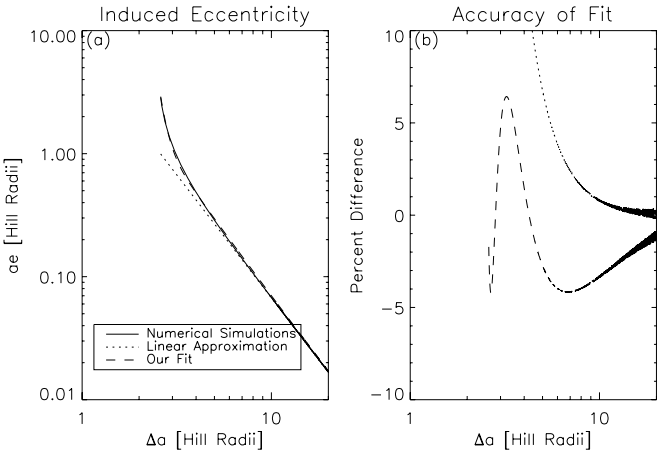

Figure 7. Relationship between the edge wave amplitude (ae) and Δa (both scaled by the Hill radius) for the numerical models (solid line), our fit to this model (dashed), and the linear, analytic model (dotted) is shown in (a). In (b) we plot the difference between the numerical model and our fit (in percent). The fit (see text for functional form) is generally within 5% of the numerical model and never more than ~ 7 % different, a significant improvement on the linear relationship previously used for edge waves. The difference between the numerical model and the linear relationship is plotted in (b) as a dotted line.

Our final fit (where all variables are in Hill radii) is

$$ae = \left(\frac{6.72}{(\Delta a)^2} + \frac{4}{(\Delta a)^3} + \frac{1.1 \times 10^6}{(\Delta a)^{14}} \right) a. \qquad (18)$$

It is apparent that our fit, although imperfect, does much better matching the numerical results for most of the range than the older model does.

The first term—which dominates through most of the range of Δa of interest here—is proportional to $(\Delta a)^{-2}$, as predicted by the earlier analytical work (Julian & Toomre 1966). This accurately reflects the slope of the large, nearly linear portion of Figure 7. The linear, analytic model for the interaction is plotted as a dotted line for comparison and it is readily apparent that it is accurate for $\Delta a \gtrsim 5$, but definitely not below that limit. The Pan–Encke interaction falls above the cutoff for a good fit—which explains why the numerical models do not suggest any significant revision in the mass of Pan is required—but Daphnis–Keeler are clearly below this limit and it is likely that any future moon-edge systems discovered will be, too.

We can reintroduce units to Equation (18) to get an expression that relates a, $\Delta a'$, μ, and e (where $\Delta a'$ and a are not scaled by the Hill radius):

$$ae = \frac{2.24a^3}{(\Delta a')^2}\mu + \frac{1.1a^4}{(\Delta a')^3}\mu^{4/3} + \frac{4.5 \times 10^3 a^15}{(\Delta a')^{14}}\mu^5. \qquad (19)$$

This equation reduces to the analytically derived equation (Equation (1)) in the case where Δa is large and the first term dominates.

Unfortunately, this equation cannot be solved for μ in closed form, but it can be numerically solved for a given measured ae and $\Delta a'$. Figures 5 and 6 show this fit compared with the numerical and the linear models for the Encke and Keeler Gaps. For Pan, the linear model predicts a departure from the moon-mass of 1.1% from the numerical models while our fit predicts a mass 3.6% from the numerical model. Contrary to what we might have expected, our fit actually does slightly worse in this range. However, the differences between the original estimate and the results of our fit are small—equivalent to a

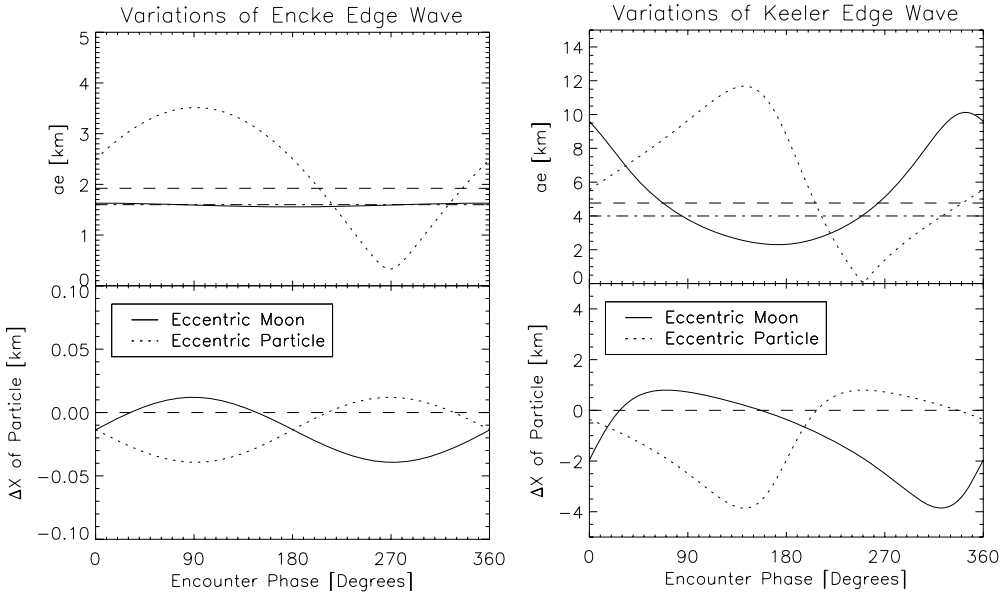

Figure 8. Variations of edge wave amplitude (ae) and the edge's shift in semimajor axis (ΔX) as a function of encounter phase for both the Encke and Keeler Gaps. The solid lines show the results when the moon's orbit is eccentric and the edge is initially circular while the dotted lines show the results in the case when the moon's orbit is circular and the edge particles have initial orbital eccentricities. The same eccentricity—1.44×10^{-5} for Pan and 3.31×10^{-5} for Daphnis (Jacobson et al. 2008)—was used for both edge and moon to facilitate comparisons within a given moon–gap arrangement. Each curve represents the results of 360 integrations. The dashed lines in the ae plots give the radial variations due to this eccentricity and the dot-dashed lines give the observed amplitudes of the edge waves. The dashed line in the lower plots merely indicates 0 (no change).

60 m error in the measurement of the edge wave amplitude or less, less than the resolution in the available images (of order 1 km pixel^{-1})—so the degradation is realistically not a concern. Daphnis is another matter: we improve our mass estimate from 30% discrepancy to only 5%. Given such a large improvement, the fit's utility for the smaller moons is apparent.

4. EFFECT OF ORBITAL ECCENTRICITIES

We are now ready to complicate the simple picture presented above by freeing more parameters. First, we will examine how allowing either the particle or the moon to have an orbital eccentricity affects the edge waves. To keep the analysis tractable, we will only allow nonzero eccentricities for one body at a time. To facilitate comparison between the two cases, we will give the particles the same orbital eccentricity as the moon. Note that this eccentricity is higher than the random component usually found in dense rings (which is $\ll 1 \times 10^{-6}$), but may be reasonable if the entire edge has a coherent variation to it, perhaps memory from the last satellite passage or perhaps from another resonant perturber.

For small gaps, such as the Keeler Gap, eccentricities are likely to be important. Although the edges most likely lose any memory of the previous encounter between successive passages via particle–particle interactions—the synodic period between the Keeler Gap edges and Daphnis is eight years, which should be ample time for a process that takes a few tens of orbits—even a small orbital eccentricity would cause the moon to move significantly closer to and farther from the gap edges over an orbit. Moreover, the Keeler Gap shows significant temporal variations in the edge waves, an expected effect if Daphnis' orbit is eccentric. On the inner edge, these variations are at least partly caused by changes in Δa due to its resonance with Prometheus. However, the outer edge of the gap also shows significant temporal variations in edge wave amplitudes despite having only small changes in Δa.

Examining our simulation results, we start with Pan having an orbital eccentricity of 1.44×10^{-5} (Jacobson et al. 2008). We examine variations in both induced particle amplitudes and shift in semimajor axis as functions of phase of the moon or of the particle when the two bodies' mean longitudes are equal (encounter phase). It is important to remember that the value of ae for an individual particle is no longer necessarily the edge wave amplitude, in this case. This is because the entire edge is composed of particles that encountered the moon at every possible phase. Since there is considerable variation in the postencounter ae of the particles, the resulting edge wave amplitude depends on all of the induced eccentricities as well as the particle phases at the time of observation. (Figure 9, which displays the four snapshots of the same edge at different times, shows how particles at a variety of phases combine to make a gestalt edge which could not be predicted without tracing the locations of all the particles at each time.)

Figure 8 (left side) shows these variations for an eccentrically orbiting Pan in a solid line and an eccentrically orbiting ring particle in a dotted line. In the upper (amplitude) plot, the dashed line shows ae, the amplitude of the eccentric excursion of the moon or the ring particle's initial amplitude. The dot-dashed line indicates the observed value of the edge wave amplitude, while the dashed line in the lower plot indicates $\Delta X = 0$ for reference.

Things are much as one might expect in the Pan–Encke case. For both cases, ΔX curves are identical but shifted 180° phase, as expected.[5] The changes in semimajor axis vary sinusoidally about −0.01 km with the largest shifts occurring around 90° or 270°. At these phases the moon or the particle is moving purely radially in its epicycle, resulting in the largest asymmetry in the

[5] The shift comes about because of the coordinate system: the moon and particle are closest together when the particle is at 180° phase (apoapse) or when the moon's phase is 0° (periapse). This naturally leads to the two curves being shifted by half a cycle.

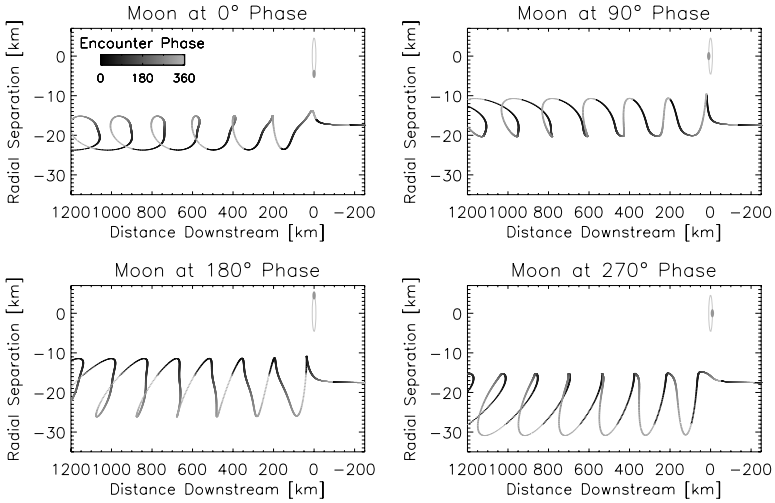

Figure 9. Locations of the Keeler-edge particles at four orbital phases of Daphnis. Darkness of the particles indicates their encounter phases. Note that this does not take into account collisions, either between particles on this Δa or with particles with different Δa's. The ellipse at the upper right of each plot shows the eccentric epicycle of Daphnis, the dot on the ellipse shows the position of Daphnis at each time. The vertical dimension of these plots has been stretched to show the radial variations.

distance between bodies—and therefore the tangential force—pre- and postencounter.

In the Pan–Encke case of $e_m(t = 0) > 0$ and $e_p(t = 0) = 0$, the edge wave amplitude varies about the ae for the circular–circular case discussed in Section 3. The largest particle orbital eccentricity is imparted when the moon is closest to the edge (a phase of 0°) and the smallest eccentricity comes about when the moon is farthest from the edge (a phase of 180°). This is precisely what we expect from a gravitational encounter: nearer encounters have larger effects, all other things being equal. However, the variations, while apparent, are small and nearly symmetrical about the circular–circular case. This suggests that we could use the mean ae—either averaged over an orbit of Pan or simply averaged between the two gap-edges at the same time—in the circular–circular formula and get an accurate mass measurement. In fact, the variations with phase are sufficiently small that even without such averaging, the mass estimate would be sufficiently accurate for almost all purposes. The real Encke–Pan system most closely resembles this case since the edges of the Encke Gap have only small radial variations relative to Pan's eccentric variations (pre-encounter). Thus, there is little concern about using the simpler circular–circular model to determine Pan's mass.

When $e_m(t = 0) = 0$ and $e_p(t = 0) > 0$ (still considering only Pan–Encke), the particle's initial orbital eccentricity dominates the postencounter ae, at least for this relatively large eccentricity. The particle's initial eccentricity is more than twice what is induced in the circular–circular case, so this should come as no surprise. Varying the encounter phase induces a nonsinusoidal variation about the initial ae with an amplitude of 1.5 km. The largest increase in ae occurs near 90° encounter phase where the particle is moving straight toward the moon so that the moon's acceleration on the particle acts to increase this velocity. The force is almost purely radial around the time of closest encounter, meaning that there is very little change in the particle's semimajor axis. In this situation, increasing the radial velocity can only go toward increasing the eccentricity of the particle, so the induced eccentricity is greatest here. The reverse is true at 270°, leading to a minimum in ae postencounter.

Unfortunately, the difference in the mean ae postencounter and the ae pre-encounter is less than 150 m, about 3% of the amplitude. It would be very difficult to measure this change in amplitude, making it unlikely that we could reasonably extract a mass estimate in this case.

The Keeler–Daphnis system presents a very different picture from the Pan–Encke system. Recent fits to Daphnis' orbit—based on nearly three years of Cassini images—reveal an orbital eccentricity of $(3.31 \pm 0.62) \times 10^{-5}$ (Jacobson et al. 2008), more than twice that of Pan. This comes as something of a surprise since any significant eccentricity might be expected to damp out due to ring–moon interactions. However, there is additional reason to believe that Daphnis truly does have substantial eccentricity: the amplitude of the waves on the outer edge of the Keeler gap show significant time variability. This is another signature of an eccentric moon. (The inner edge also shows time variability, but it is difficult to determine how much of this is due to Daphnis' eccentricity and how much is due to the large variability in Δa and pre-encounter e on this edge due to resonance with Prometheus.)

The measured amplitudes of the edge waves used in Section 3 (1.8–5.6 km) are similar to Daphnis' 4.5 km eccentric variation, so the resultant edge waves have similar amplitudes whether the moon or the particle has the eccentric orbit pre-encounter—in contrast with Pan–Encke. The shapes of the two amplitude curves are no longer identical, though. When $e_m(t = 0) > 0$ and $e_p(t = 0) = 0$, there is a broad minimum in amplitude with a relatively symmetrical, narrow peak ($\sim 60°$ FWHM for the peak). The broad minimum region and sharp peak indicates the strong dependence on distance of the "kick" given to the particle. Not only are the particle and moon significantly closer together when the moon is near periapse, the particle's response (which is to move even closer to the moon) amplifies this effect. This is not seen in the Encke Gap models because the relative change in the particle's distance from the moon is trivial, but with the narrower Keeler Gap even a 1 km shift is significant.

The peak of the curve no longer occurs at 90° as in the Pan–Encke case, but now at −30° phase. This can be most easily ascribed to the large shift in semimajor axis that occurs coincident with the maximum induced eccentricity. A rapid (meaning timescales less than an orbit), large shift in osculating a must accompany a large increase in the osculating e for a circular orbit: since the particle cannot move very far in a short

time, the particle and guiding center separate, resulting in a large eccentricity. This is most easily seen via Equation (12), setting the pre-encounter e to zero and considering what happens when the postencounter X is very different from the pre-encounter value. Since x cannot undergo a large change over a short time (although if the particle were to rapidly move, this would imply a large eccentricity which is what we claim is the outcome in any case), the only response that the particle can make is to acquire a substantial osculating eccentricity.

By contrast, when $e_m(t = 0) = 0$ and $e_p(t = 0) > 0$, the minimum is much narrower and the overall curve is now obviously asymmetrical. The asymmetry can ultimately be ascribed to two effects, each controlling one extremum. The first effect is, as discussed above, the role of the changing semimajor axis in setting the location of the largest postencounter eccentricity. The second, which sets the minimum postencounter particle eccentricity, is the damping of the eccentricity when the particle is moving away from the moon at closest approach (discussed above to explain Pan's effects). The first-order predictions for the locations of these two extrema are 180° and 270°. Since these are not 180° apart in phase, the behavior must change more rapidly with phase between 180° and 270° than in the rest of the range.

The problem of collisions in this case is in fact worse than just suggested. Because of the large radial displacements experienced by the particles on the edge, their trajectories cross far into the ring interior (up to 15 km, from Figure 9). Particles that are approximately 15 km from the edge are six or more Hill radii from the moon. As such, they should experience small perturbations from the passing moon, akin to those experienced by particles in the Pan–Encke case. For these particles, their downstream trajectories are not much different from their upstream trajectories and they are therefore in the path of the highly perturbed edge particles when the latter are near their periapses. Collisions are inevitable in this situation and their expected effect is to damp the amplitude of the edge waves more rapidly.

Unfortunately, test-body simulations themselves fail for large induced edge waves, such as those we have simulated here for the Keeler gap. The problem is that collisions become important for all but the most tenuous of ring-edges in this case. Figure 9 shows our snapshots of the Keeler edge at four orbital phases of Daphnis. Two things are apparent from these plots. First, there is substantial time-variation in the edge—both in morphology and in amplitude. Second, the edge becomes self-intersecting (i.e., the predicted edge morphology requires the particles to pass through each other) after as little as one orbit (locations in Figure 9 that show cusps generally reveal self-intersection upon close inspection)—much less for some phases. In this case, collisions must occur much earlier than in the circular–circular cases. These collisions almost certainly make large changes to the orbits of the individual particles and so the downstream trajectories are all suspect.

5. ORBITAL INCLINATIONS

The remaining parameter to examine in these numerical methods is orbital inclination. Fortunately, the parameter space in inclination is smaller than for eccentricity: we can assume that either the moon or the ring defines the reference plane, leaving just one inclination and vertical phase to consider. So, without loss of generality, we will take the ring's pre-encounter plane to be the reference plane. Pan's measured inclination (Jacobson et al. 2008) is $0\overset{\circ}{.}0001 \pm 0\overset{\circ}{.}0004$, not statistically different from

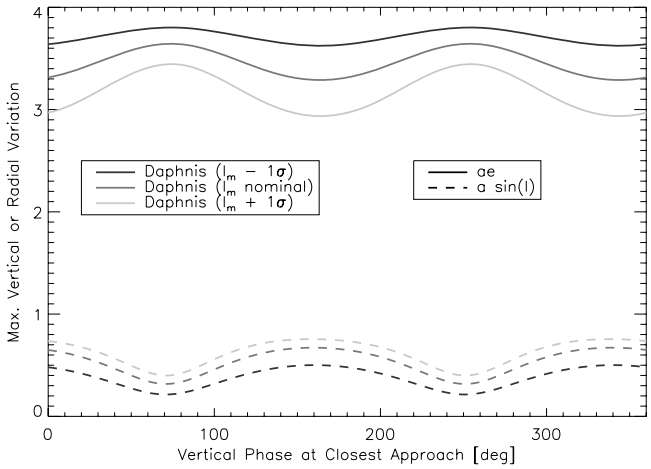

Figure 10. Variations of edge wave amplitude (ae, in solid lines) and postencounter vertical oscillations ($a \sin(I)$, in dotted lines) on the Keeler Gap with Daphnis' vertical phase at encounter. Three different possible inclinations of Daphnis are used: the nominal value from Jacobson et al. (2008), as well as this value plus 1σ and minus 1σ. Each curve represents the results of 360 simulations.

$0\overset{\circ}{.}0005$, corresponds to a vertical amplitude of 1.1 km (0.064 Hill radii) and our models of edge wave behavior using this inclination for Pan are indistinguishable from the uninclined case. We will therefore not treat the Pan–Encke case any further in this section.

Daphnis' inclination is substantially larger, $0\overset{\circ}{.}0036 \pm 0\overset{\circ}{.}0013$, corresponding to 8.6 km (1.7 Hill radii) vertical oscillations (ring-plane to peak distance), about twice to the size of the moon itself (Porco et al. 2007), and about half Δa. Figure 10 presents the results of varying Daphnis' vertical phase at encounter for three models: the nominal value of I_m from Jacobson et al. (2008), the nominal value plus 1σ, and the nominal value minus 1σ. The resulting variations in the edge wave amplitude (ae) and vertical amplitude ($a \sin(i)$) are shown for all three cases. Because the magnitudes of the forces do not depend on the sign of z_m, all the curves show an $m = 2$ symmetry.

Although there is an obvious variation in ae with encounter phase, the effect is only 5% for the nominal case, 8% for the largest inclination, and 2% for the smallest. The decreasing amplitude of the edge waves is of somewhat greater concern for mass-determination; in the nominal case, the edge waves have an amplitude 0.5 km smaller than the coplanar case, while for the smaller I they are 0.3 km smaller and for the larger case the decrease is 0.8 km. The decrease in ae is caused by the decreased magnitude of the force near closest approach due to the larger moon–particle separation. The decrease in ae for Daphnis would result in a mass estimate which is 10% (nominal), 4% (smallest-I_m), or 16% (largest-I_m) below the actual moon mass if the effects of I_m are not considered.

The vertical forces from the moon also induce a postencounter inclination in the particles, also found by Kolvoord & Burns (1992). As Figure 10 shows, the induced inclinations are modest, averaging 0.5 km for the nominal I_m. This is much smaller than the moon's vertical variation, but much, much larger than the ring's inferred vertical thickness of 10 m (Colwell et al. 2006; Porco et al. 2008). As with ae, the extrema occur around 0°/90°/180°/270°,[6] with the biggest induced inclinations near 0° and 180° where the moon is at its largest vertical extent.

[6] The locations are shifted by ≈ 20° in much the same manner as for the eccentric moons.

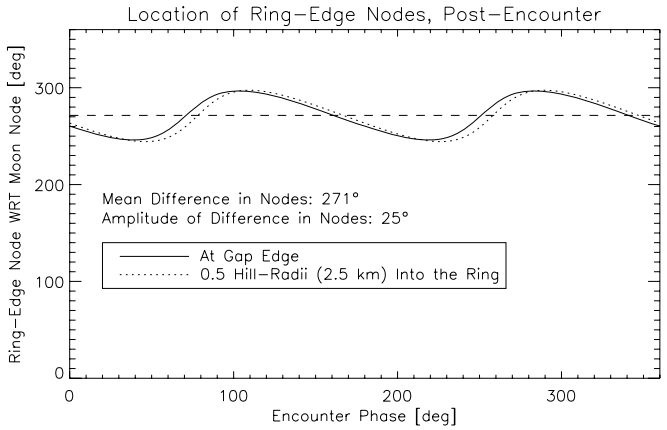

Figure 11. Location of the ascending node of the ring-edge (solid curve) postencounter, relative to Daphnis' ascending node. Daphnis' inclination is taken to be 0.°0036, the nominal value in Jacobson et al. (2008), but we find that no variation is seen for the other two inclinations used in Figure 10. Also shown is the location of the ascending node for the annulus of ring 0.5 R_H farther from the moon for comparison. The dashed line shows the mean value longitude of the node.

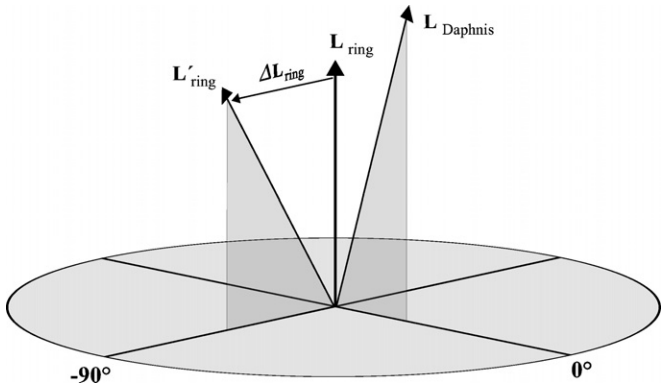

Figure 12. Orientation of the moon's angular momentum vector ($\mathbf{L}_{\rm Daphnis}$) and the ring's pre- ($\mathbf{L}_{\rm ring}$) and postencounter ($\mathbf{L}'_{\rm ring}$) angular momentum vectors. The magnitudes of the vectors are not to scale and the angle of separation from the z-axis has been exaggerated for clarity.

(This need not necessarily be the case, however. The maximum vertical force on the ring edge occurs for $z_m = \Delta a/\sqrt{2}$, requiring $I_m \geqslant 0.°0052$ for Daphnis, slightly larger than the largest value of I_m modeled here.)

The effects of the ring's induced inclination on Daphnis depend on the orientation of the ring's orbital tilt. In particular, if the longitudes of the particles' ascending nodes are distributed around all 360° longitude, the torques will cancel and the moon will experience no net change in inclination or location of its node. On the other hand, if the ascending nodes are all near the same longitude, there exists a potentially large torque (see discussion below) on the moon's orbit that could change the inclination or alter the orientation of the orbit. Figure 11 shows the location of the ascending node of the ring-edge with respect to Daphnis' ascending node as a function of encounter phase for the nominal inclination found by Jacobson et al. (2008). The other two cases examined in Figure 10 were unnecessary as all three curves lie precisely on top of each other, indicating that the inclination of the moon is not important to this effect. Also shown is the postencounter ascending node for an annulus of ring 0.5 R_H farther into the ring (away from the moon). The location of the node in this case is almost the same as at the ring-edge. The ring material's node trails the moon's by almost 90° after the encounter, with only a small variation of ±25°. This has at least two important implications.

The first implication of this node alignment is that the overall ring-edge will be oriented in the same manner (even though the apparent tilt would seem to vary as particles with different inclinations pass through maximum vertical extent). In this case, particles will be moving in the same direction even as the different orbits shear past each other, resulting in gentle collisions. The edge's inclination could persist for many orbits in this state. This additionally suggests that our test-particle models are adequate for interpreting the edge waves in this case.

Second, the ring's total angular momentum will have a net change postencounter, both in orientation and in magnitude. Conservation of the system's angular momentum requires that torques on the ring be balanced by torques on the moon, thus Daphnis' orbit inevitably changes as well as the ring's. If Daphnis' pre-encounter angular momentum vector is tilted (by 0.0036°) from the z-axis toward 0° longitude—meaning that the ascending node is 90°, the ring's postencounter angular momentum vector tilts toward −88.°6. (The total z-component of the angular momentum will not change since the inner and outer gap-edges move in opposite directions.) Figure 12 shows a diagram of the angular momentum vectors. As a result of the encounter, Daphnis' ascending node must shift around toward 180°, although how far in that direction the vector moves depends on the mass of the ring annulus which participates in this interaction.

In addition to precessing the longitude of Daphnis' ascending node, a massive ring will also alter the inclination of the moon. The induced ring inclination (magnitude and orientation) can be used to find the change in the ring's angular momentum vector. This change must be balanced by a change in the moon's angular momentum, allowing us to compute the change in the moon's inclination. Whether the inclination of the moon increases or decreases depends not only on the final orbits of the ring particles, but can also depend on how much ring-mass interacts with the moon at any given instant since this mass sets the magnitude of the torque on the ring. A suitable order-of-magnitude estimate of this mass may be found by estimating the radial and longitudinal dimensions of the interacting patch of ring. For the radial width of this patch, we can use the distance into the ring where the induced ring inclination drops to half the induced inclination at the edge, while for the longitudinal scale one wavelength at the edge (given by $3\pi\Delta a$) would be suitable. For Keeler–Daphnis, the radial component is approximately 2.5 km and the $3\pi\Delta a$ is about 165 km. For a surface mass density of 30 g cm^{-2}, a value consistent with what is measured by density waves in this region (Tiscareno et al. 2007), the combined mass of the inner and outer edges of the Keeler Gap are about 0.0014 times the mass of Daphnis. Using this value to compute the rate of change of Daphnis' inclination we find that Daphnis' inclination will be damped. However, we find that changing our assumptions about the interacting mass only slightly (enough to yield a 10% change in the mass of the ring patch) will change the sign of this change so that excitation becomes damping. Considering the uncertainties in this calculation, we therefore refrain from giving a prediction for the damping or excitation timescale.

Our result that Daphnis–Keeler is close to the critical point where damping and excitation are in balance is consistent with the results of Hahn (2007) who found that the inclination-damping effects of the secular perturbations modeled analyt-

ically in that work nearly balanced the inclination-exciting effects of vertical resonances studied (also analytically) by Borderies et al. (1984). These treatments are likely to be more accurate than our numerical models at including the torques from ring components far upstream or downstream of the moon as they account for the curvature of the rings. We can use the rates of change for moon inclinations from both excitation and damping given in the aforementioned works to derive an estimated timescale for inclination damping or excitation. The rate of inclination excitation for a moon due to vertical resonances is

$$\left(\frac{\dot{I}_m}{I_m}\right)_{\rm res} = \frac{g\mu_m\mu_d n}{\Delta^4} \tag{20}$$

(Ward & Hahn 2003), where $g = 0.0118$, $\Delta = \Delta a/a$, and μ_d is the ratio of the mass of the ring to the mass of the planet. These effects are countered by secular perturbations that damp the inclination at the rate

$$\left(\frac{\dot{I}_m}{I_m}\right)_{\rm sec} = -\frac{C(|k_0|a\Delta)}{2\pi}\frac{\mu}{\Delta^2}n \tag{21}$$

(Hahn 2007), where k_0 is the initial wavenumber at the disk's inner edge and the function, $C(|k_0|a\Delta)$ is plotted in Hahn (2007).

These rates can be added to give a total rate of change of the moon's inclination:

$$\left(\frac{\dot{I}_m}{I_m}\right)_{\rm total} = \frac{\mu n}{\Delta^2}\left(\frac{g\mu_d}{\Delta^2} - \frac{C(|k_0|a\Delta)}{2\pi}\right). \tag{22}$$

This can be inverted to give a timescale for inclination damping/excitation:

$$\tau_{\rm inclination} = \frac{\Delta^2}{\mu n\left|\frac{g\mu_d}{\Delta^2} - \frac{C(|k_0|a\Delta)}{2\pi}\right|}. \tag{23}$$

Hahn (2007) found that $|k_0|a\Delta \sim 1$ for the Keeler–Daphnis system so that $C(|k_0|a\Delta) \sim 0.3$. So, using $\mu_d \sim 5 \times 10^{-8}$ (the mass of the A ring), Daphnis should experience inclination damping with a timescale of order 1000 years.

6. ECCENTRIC, INCLINED MOON

For Daphnis' orbit, both orbital inclination and eccentricity are substantial compared to the size of the Keeler Gap; we have shown that both effects separately cause large temporal variations in the ring's postencounter characteristics (ae, $a\sin(I)$, ΔX, etc.). In this section, we examine the effects of both the moon's inclination and its eccentricity together. We will continue to use Daphnis' measured inclination and eccentricity (Jacobson et al. 2008) and the mass we found in Section 3. Two free parameters remain in this problem, however: the moon's epicyclic phase at encounter and the moon's vertical phase at encounter. Because of Saturn's oblateness, these two phases do not have constant separations in time but rather, due to regression of the node and precession of the periapse, shift relative to each other by 6° day^{-1} (Jacobson et al. 2008). For this reason, models for the inclined, eccentric moon must be run at a full sampling of both encounter phases.

Figure 13 shows the effects on the ring's postencounter ae due to the combination of Daphnis' eccentricity and inclination at the full range of both encounter phases. One effect of adding the moon's inclination has been to shrink the range of ae from

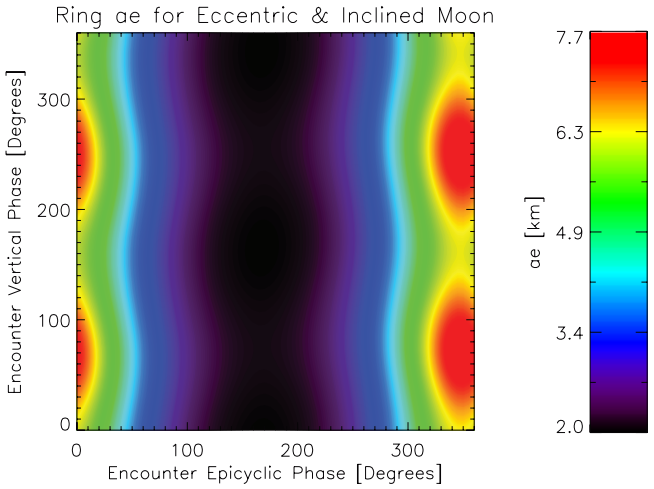

Figure 13. The ring edge's postencounter ae due to the combined effects of Daphnis' orbital inclination and eccentricity. Shown here are the results of 5184 cases run.

the cases where only the moon's eccentricity was included (Figure 8); in the previous case, ae was as large as 10.3 km, whereas here it never exceeds 7.7 km. This is presumably again because of the fact that—due to the inclination—the moon spends much of its time around the encounter farther away from the particles than in the coplanar case, just as was found in Section 5.

More significantly, the variations in ae suggest that this problem can be treated as mathematically separable into the variation with vertical phase and the variation with epicyclic phase: $ae = cZ(\zeta)\Phi(\phi)$, where $Z(\zeta)$ is a function of the vertical phase alone, $\Phi(\phi)$ is a function of the epicyclic phase only, and c is a constant.

As a crude guess at suitable functional behaviors, we take $Z(\zeta)$ to go like the ae in Figure 10 divided by 4 km and $\Phi(\phi)$ similarly to go like the ae in Figure 8 divide 4 km. The logic for these choices is that each function represents the ratio of the simulated ae to the ae for the coplanar, circular–circular case in Section 3. Under the simplifying assumption that each effect increases or decreases ae independently, the product of these ratios is the ratio of ae for the combined case to the 4 km coplanar, circular–circular case. Choosing $c = 4$ km yields a prediction for ae which qualitatively looks similar to Figure 13. Quantitatively, the peak ae is 9 km in this model, a bit larger than in the more accurate simulation, but the minimum ae is still 2 km.

The same overall behavior in phase space is seen in the particles' induced inclinations in the same suite of simulations (Figure 14). There are differences, however. In particular, the range of induced inclinations has *increased* here from the circular, inclined case of Section 5, whereas the range of ae in Figure 13 decreases from the eccentric, coplanar case. The minimum induced vertical amplitude in the gap edge is now 0.2 km—about half what it was in the circular, inclined models—and the maximum value has jumped up to 1.7 km, over a factor of 2 larger than the largest amplitudes seen in the earlier models. This is due to the fact that adding the moon's orbital eccentricity can either increase or decrease the gap–moon distance and therefore decrease or increase the magnitude of the forcing.

Although it is generally difficult to measure small vertical displacements on the edges of gaps, in 2009 (as Saturn approached

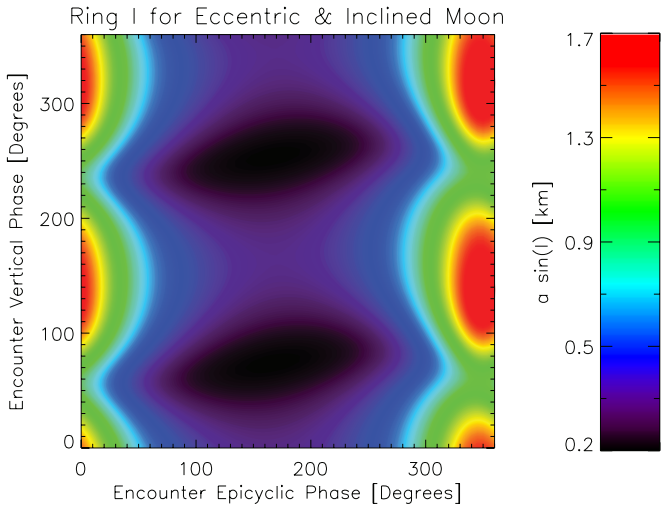

Figure 14. The ring edge's postencounter $a \sin(I)$ due to the combined effects of Daphnis' orbital inclination and eccentricity. Shown here are the results of the same 5184 cases shown in Figure 13.

equinox) Cassini acquired images such as Figure 15 showing the shadows of vertically displaced ring features cast on the rings. In this case, shadows of the inner and outer edges of the Keeler Gap are projected on the A ring interior to the gap. (Note that Daphnis is also casting a shadow in this image, conveniently giving the orientation of the Sun.) The shadows appear intermittently along the gap edge, suggesting that the gap edge undulates vertically after encountering the moon. Also, no shadows appear before the edge encounters Daphnis, strongly pointing to Daphnis as the cause of the vertical displacement. The subsolar latitude on Saturn at the time of this observation was $-1\overset{\circ}{.}2$, so vertical features cast shadows 47 times their vertical displacement. The shadows in this image (which are 50–75 km long) indicate that the gap edge is vertically perturbed between 1 and 1.5 km.

To understand the morphology of vertical features casting these shadows, consider Figure 16. Similar to Figure 9, each panel shows a snapshot of the vertical profile of the edge at one time. In this case, we need to consider not only the moon's orbital phase, but also the difference between the longitudes of Daphnis' node and pericenter, since (as Figures 13 and 14 show) both affect the morphology of the edge. Luckily, the $m = 2$ symmetry in the moon's vertical forcing of the ring means that we need only examine half of a Daphnis orbit and half of the range of possible differences in moon node and pericenter longitudes to sample all possible morphologies. Figure 16 shows that some parts of the gap edge are perturbed to much higher inclinations than other portions, creating peaks and valleys along the edge. The peaks will produce much longer shadows than the valleys, as in Figure 15. (Shadows of the valleys may even be too short to be visible with limited resolution.) Also, as the particles move downstream, the vertical peaks broaden and begin to merge due to the variations in ΔX. (The same effect was seen in Figure 16.) In Saturn's rings, this should lead to enhanced collisions and therefore damping of the vertical structure, as well as broadening of the peaks.

This effect is exactly what is seen in Figure 15 as the downstream shadows are broader and shorter than the initial long, sharp shadows. The inferred vertical height of the features, between 1 and 1.5 km, is also consistent with the amplitudes of waves seen in Figure 16.

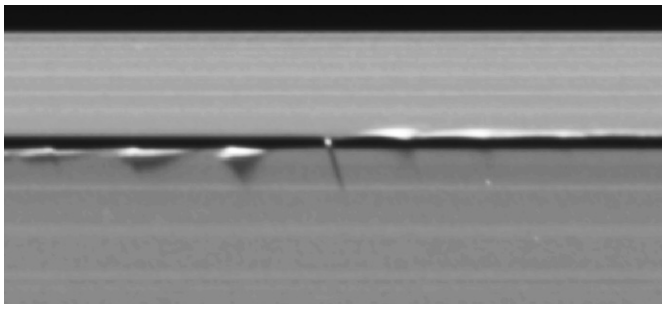

Figure 15. Cassini ISS image acquired on 2009 May 24 of Daphnis and the Keeler gap edge showing shadows cast by both Daphnis and the perturbed edge of the Keeler gap. Shadows from the outer edge of the gap do no appear as they are cast into the empty gap. The subsolar latitude during this observation was $-1\overset{\circ}{.}2$. The Cassini spacecraft was on the south (lit) face of the rings when this image was taken, so the shadows are seen through the A ring. The image has been reprojected, as with Figure 3, and contrast-enhanced to better reveal the shadows (NASA/JPL/CICLOPS/SSI).

It is possible that the shadows are instead being cast by particles which have been vertically "splashed" up during the compressional phase of the edge waves radial motion (Borderies et al. 1983; Lewis & Stewart 2000). However, there are other places in the rings, such as the outer edge of the A ring and the Encke gap, where radial compression due to the perturbing effects of a moon does not produce visible shadows in the equinox geometry, and therefore we infer that no large vertical displacements arising from splashing exist at these locations. We conclude that the vertical features here are more likely due to out-of-plane perturbations from Daphnis.

7. CONCLUSIONS

It has long been known that edge waves produced by moons embedded in ring gaps can be used to extract the moon's properties. The traditional method has relied on an analytically derived linear formula which relates moon-mass to wave amplitude. We have shown, via our numerical models, that this method is sufficiently accurate to model the case of Pan, where the edge waves and eccentric variations of the moon are both much smaller than the gap size so that the impulse approximation is fully valid. However, for the Daphnis–Keeler system, the gap is sufficiently narrow and the edge waves sufficiently large so that the analytic expression is no longer valid. In this case, we see that even for the relatively "well behaved" system with initially circular orbits, the mass estimates offered by the analytic expression overestimates the mass of Daphnis by $\sim$ 30%. Since other gaps in Saturn's rings which are focuses of satellite searches are also narrow, such errors are expected to plague the analysis of any yet-to-be-discovered ring–moons in those gaps.

To simplify the process of determining a moon mass from the edge waves, we have fit an analytic expression to our numerical models. Although our fit is not as elegant as the older linear approximation, it has the advantage of agreeing with the numerical results to within 7%, even for small moon/edge separations. This represents a significant improvement in accuracy for moons in narrow gaps.

We have also shown that Pan's eccentricity and inclination do not introduce any significant difficulties for recovering its mass from the edge waves on the Encke Gap. Unfortunately, if Daphnis' eccentricity is as high as is currently believed, there will be major variations in the edge waves over one full orbit of Daphnis (Lewis & Stewart 2006). Worse, because of the

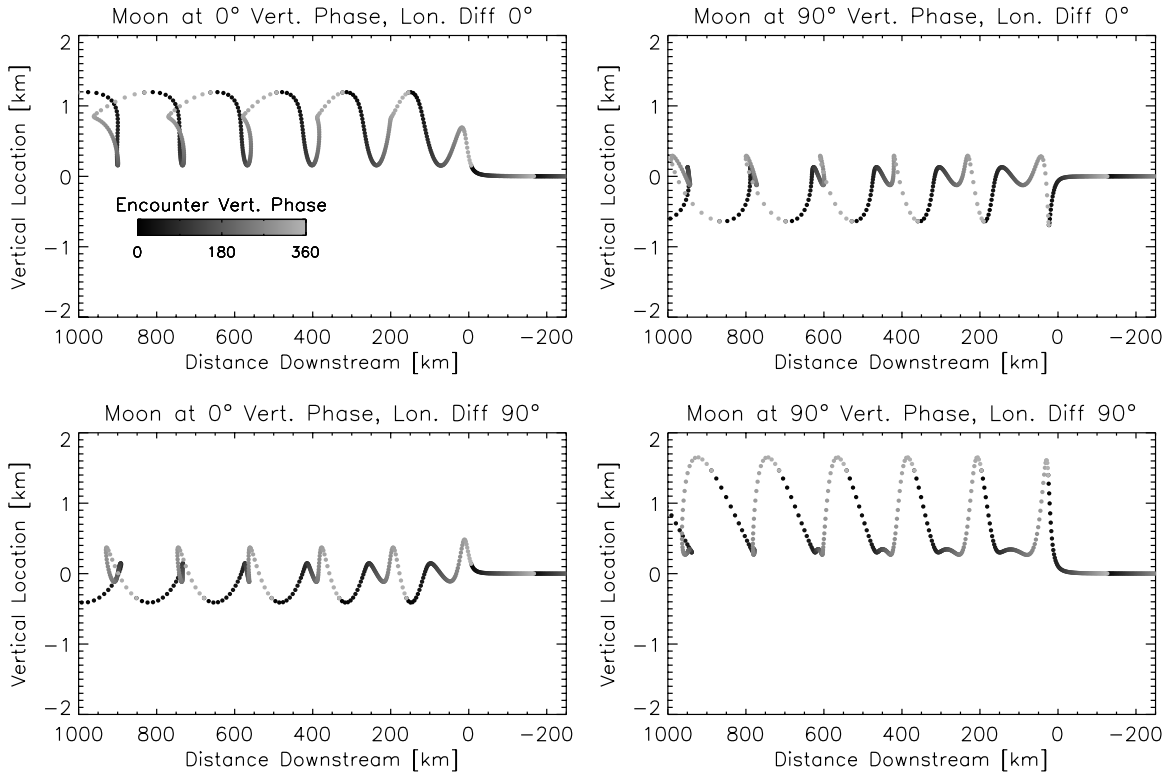

Figure 16. Snapshots of the vertical structure on the edge of Keeler Gap from the same runs used in Figures 13 and 14. Shading of points indicates the vertical phase of Daphnis at the time of the particles' closest approach. Top panels show ring profiles at a time when the moon's ascending node and pericenter are at the same longitude. Lower panels show a time when the moon's node and pericenter are separated by 90 degrees. Left panels are snapshots when the moon is at 0 degrees vertical phase, right panels are taken at a time when the moon is at 90 degrees phase.

large changes in the particles' semimajor axes and the large eccentricities that accompany these shifts, collisions between particles owing to intersecting streamlines play a major role in the observed edge wave amplitudes. As a result, the only sensible way to accurately determine the mass of such a body is through *N*-body simulations, an expensive approach both in computational resources and in time. But even in this limit, we believe that our fit for the mass can be used to give *N*-body modelers an improved starting point for their simulations, saving time and computation.

Unfortunately, our work indicates that if an edge approaches a moon with a large, existing eccentricity (perhaps driven by a resonance with another body), the amplitude of these variations in the particles' eccentricities will dominate the postencounter waves to such an extent that determining the moon's mass may be impossible. But although both known gap–moons are located in gaps whose edges show structure upstream of the moons (Tiscareno et al. 2005), except in the case of the inner edge of the Keeler Gap, the amplitude of these upstream structures is small compared to the downstream induced edge wave amplitudes. In such cases, it is still feasible to determine the moons' masses from the downstream edge waves, though there is no guarantee that gap–moons to be discovered will be so well behaved.

In the case of a significantly inclined moon such as Daphnis, the moon's vertical excursions also cause temporal variations in the edge wave amplitudes as well as causing an overall decrease in edge wave amplitudes at all times. In addition, the moon's out-of-plane forces on the ring induce an inclination in the edge. The induced inclination is also time-variable, although the variations are relatively small. Although the induced inclination of the ring-edge is much smaller than the moon's inclination, it can cause projection effects in observations. For example, the viewing geometry of the discovery images of Daphnis from 2005 May (when spacecraft elevation was 20° above the ring plane) leads to a projection effect of up to 1.5 km, substantial compared to the ≈ 2–6 km amplitude of the edge waves. These projection effects are large enough to confuse the measurements of the in-plane edge wave amplitudes. The ring also applies a torque on the moon that can either damp or excite the moon's inclination, depending on the particular situation. In the case of Daphnis, we find that the damping and exciting tendencies are nearly in balance, in agreement with Hahn (2007).

Our work shows that in optimal gap–moon cases (e.g., where the eccentric and vertical excursions of the moon are small compared to the gap half-width), simple test-body dynamics should suffice for the purpose of mass-determination for the moon. However, in cases where the moon is eccentric or inclined, particle–particle interactions are expected to become significant and therefore *N*-body simulations are required. While such simulations are already being undertaken (Lewis & Stewart 2006; Perrine & Richardson 2006), it is hoped that our work will provide a survey of the parameter space to help reduce the number of expensive *N*-body simulations required in future studies.

The research presented in this paper was primarily supported by NASA grant CDAP NNX08AP84G and by the Cassini mission. The authors also thank Joe Burns and Joe Hahn for their helpful comments and suggestions on this paper.

REFERENCES

Borderies, N., Goldreich, P., & Tremaine, S. 1983, Icarus, 55, 124
Borderies, N., Goldreich, P., & Tremaine, S. 1984, ApJ, 284, 429

Colwell, J. E., Esposito, L. W., & Sremcevic, M. 2006, Geophys. Res. Lett., 33, L07201
Cuzzi, J. N., & Scargle, J. D. 1985, ApJ, 292, 276
Dermott, S. F. 1984, in Planetary Rings, Dynamics of Narrow Rings (Tucson, AZ: Univ. Arizona Press), 589
Dermott, S. F., & Murray, C. D. 1981, Icarus, 48, 1
Goldreich, P., & Tremaine, S. 1982, ARA&A, 20, 249
Hahn, J. M. 2007, ApJ, 665, 856
Hill, G. W. 1878, Am. J. Math., 1, 5
Jacobson, R., & French, R. 2004, Icarus, 172, 382
Jacobson, R. A., Spitale, J., Porco, C. C., Beurle, K., Cooper, N. J., Evans, M. W., & Murray, C. D. 2008, AJ, 135, 261
Julian, W., & Toomre, A. 1966, ApJ, 146, 810
Kolvoord, R. A., & Burns, J. A. 1992, Icarus, 95, 253
Lewis, M. C., & Stewart, G. R. 2000, AJ, 110, 3295
Lewis, M. C., & Stewart, G. R. 2006, BAAS, 38, 560
Perrine, R. P., & Richardson, D. C. 2006, BAAS, 38, 560
Porco, C. C. The Cassini Imaging Team 2005, IAU Circ., 8524, 1
Porco, C. C., Thomas, P. C., Weiss, J. W., & Richardson, D. C. 2007, Science, 318, 1602
Porco, C. C., Weiss, J. W., Richardson, D. C., Dones, L., Quinn, T., & Throop, H. B. 2008, Simulations of the Dynamical and Light-Scattering Behavior of Saturn's Rings and the Derivation of Ring Particle and Disk Properties, AJ, 136, 2172
Porco, C. C., et al. 2004, Space Sci. Rev., 115, 363
Porco, C., et al. 2005, Science, 307, 1226
Press, W., Teukolsky, S., Vetterling, W., & Flannery, B. 2002, Numerical Recipes in C++: the Art of Scientific Computing (Cambridge: Cambridge Univ. Press)
Rosen, P. A., Tyler, G. L., Marouf, E. A., & Lissauer, J. J. 1991, Icarus, 93, 25
Showalter, M. R. 1991, Nature, 351, 709
Showalter, M. R., & Burns, J. A. 1982, Icarus, 52, 526
Showalter, M. R., Cuzzi, J. N., Marouf, E. A., & Esposito, L. W. 1986, Icarus, 66, 297
Spitale, J. N., Jacobson, R. A., Porco, C. C., & Owen, W. M., Jr. 2006, AJ, 132, 692
Stewart, G. 1991, Icarus, 94, 436
Tiscareno, M. S., Burns, J. A., Hedman, M. M., Spitale, J. N., Porco, C. C., & Murray, C. D. Cassini Imaging Team 2005, BAAS, 37, 767
Tiscareno, M. S., Burns, J. A., Nicholson, P. D., Hedman, M. M., & Porco, C. C. 2007, Icarus, 189, 14
Torrey, P. A., Tiscareno, M. S., Burns, J. A., & Porco, C. C. 2008, in AAS/Division of Dynamical Astronomy Meeting, Vol. 39, 15.19
Ward, W. R., & Hahn, J. M. 2003, AJ, 125, 3389